Applied Catalysis A, General 566 (2018) 181–189

Contents lists available at ScienceDirect

Applied Catalysis A, General

journal homepage: www.elsevier.com/locate/apcata

Surface morphology and phase stability effect of Ceria-Hafnia (CH_x) binary metal oxides on soot oxidation activity

Anjana P. Anantharaman[a], Hari Prasad Dasari[a,*], Harshini Dasari[b], G. Uday Bhaskar Babu[c]

[a] Chemical Engineering Department, National Institute of Technology Karnataka, Mangalore, 575025, India
[b] Chemical Engineering Department, Manipal Institute of Technology, Manipal Academy of Higher Education, Manipal, 576104, India
[c] Chemical Engineering Department, National Institute of Technology Warangal, Warangal 506004, India

ARTICLE INFO

Keywords:
Ceria-Hafnia
Secondary phase
Surface morphology
XRD analysis
Soot oxidation

ABSTRACT

CeO_2-HfO_2 (CH_x) binary metal oxides over whole composition range (0–100%) are synthesised using the EDTA-Citrate method and calcined at 600 °C/5 h. From XRD analysis, the sample series are classified as fluorite (F) phase for CH10-CH30, hybrid (F + M) phase for CH40-CH90 and monoclinic (M) phase for CH100 sample, respectively and the results were further confirmed using Raman spectroscopy. From SEM analysis, a clear surface morphology change is noticed for fluorite, hybrid and monoclinic phases of the CH_x binary metal oxides. Further, Selected Area Electron Diffraction (SAED) analysis also confirmed the single and hybrid phases of CH_x binary metal oxides. The soot oxidation for the CH_x binary metal oxides displayed high catalytic activity for Fluorite phase (CH10 ~ CH30) samples and a decrease in catalytic activity is noticed for the Hybrid phase (CH40 ~ CH90) samples. The change in catalytic activity coincides with the change in the surface morphology and phase change for the CH_x binary metal oxides. Among the Fluorite phase samples, CH10 sample displayed the highest catalytic activity (T_{50} = 430 °C) with higher surface area (29 m^2/g), lower particle size (26 nm), lower degree of agglomeration (ϕ = 2.8) higher surface oxygen concentration (44%). Isothermal-Time-on-stream (ITOS) analysis also showed that the CH10 sample can achieve T_{50} in a shorter time than compared to other CH_x binary metal oxides. Surface morphology and phase stability can also play as key descriptors in screening CH_x binary metal oxides for soot oxidation activity.

1. Introduction

Ceria being one of the stable oxidesof cerium, it crystallises in fluorite phase (F) (space group Fm_3m). In this structure, each cerium atom is surrounded by eight oxygen anions in tetrahedral position. During the reduction of CeO_2, mobile oxygen vacancy created aids in transport behaviour due to point defects. Oxygen release and uptake are directly related to the number and mobility of oxygen vacancies with the modification of ceria structure. Doping CeO_2 with suitable dopant cation leads to chemical modification of CeO_2 structure. Dopant addition into host lattice has the potential of lowering interatomic distance, oxygen basicity and oxygen vacancy formation energy by structural deformation. Amount of dopant and its nature influences the ease with which the dopant is substituted in the host lattice [1–3]. It is highly essential to form solid solution without segregation of secondary phase during the doping process since a solid solution improves redox coupling (Ce^{3+}/Ce^{4+}) and thus OSC is improved. Structural property of the material also influences its catalytic activity [4–6].

With the dopant addition of n- or p-type on a semiconductor material (CeO_2), a hole or an electron, respectively is formed due to the variation in electronic structure. This, in turn, reduces the oxygen vacancy formation energy of the system [3]. However, in the case of dopant with smaller ionic radii, the strain developed weakens the cation-oxygen bond strength and thus improves the oxygen vacancy formation [7,8]. Hf (0.83 Å) having lower ionic radius than Ce (0.97 Å) results in lowering of lattice parameter that enhances the lattice stress in CeO_2 [9]. Ce-Hf systems are applied in oxygen sensors [10], microelectronics [11] and catalysis such as soot oxidation [12], CO oxidation [13] and alcohol dehydration [14]. Reddy et al. [12] synthesised CeO_2-HfO_2 of 80:20 mol ratio using coprecipitation method under a calcination temperature of 500 °C/5 h, they analysed the material as catalysts for soot oxidation activity. Their results have concluded that surface area, crystallite size, oxygen vacancy and reducibility are vital factors that decide the catalytic behaviour [12].

The descriptors for catalytic activity of ceria is broadly classified as electronic and geometric descriptors as per the study by Capdevila-

* Corresponding author.
E-mail address: energyhari@nitk.edu.in (H.P. Dasari).

https://doi.org/10.1016/j.apcata.2018.08.019
Received 13 May 2018; Received in revised form 31 July 2018; Accepted 4 August 2018
Available online 22 August 2018
0926-860X/

Cortada et al. [3]. The electronic descriptors are the charge associated with the surface atoms, the basicity of surface anions and the redox term. However, the geometric descriptors are the interatomic distance of surface atom, surface co-ordination, phase cooperation and site isolation [3]. The apparent descriptors for the whole composition of binary metal oxides (CeO_2-HfO_2) in different phases could be significantly phase cooperation, where CeO_2 exists in cubic fluorite phase (F) [1] and HfO_2 in monoclinic phase (M) at a lower temperature [15]. It was proved that a single descriptor could not be fixed while studying the catalytic activity of ceria materials. Multiple descriptors exist depending upon various reaction conditions [3].

Our previous paper [16] has discussed single metal oxides as catalytic materials for soot oxidation activity. HfO_2 obtained the highest activity among the non-redox metal oxide [16]. Based on that work, we are interested in developing binary metal oxides between redox (CeO_2), and non-redox (HfO_2) having same oxidation state and widely different ionic radius and study the effect of phase segregation and its soot oxidation activity. The region in which the pure and hybrid phase separation occurs is studied using the characterisation techniques. For a system of $Ce_{1-x}Zr_xO_2$, the phase separation at x = 0.2 [17,18], x = 0.4 [8] and x = 0.5 [19] are reported previously. In case of $Ce_{1-x}Gd_xO_2$ with CeO_2 and Gd_2O_3 both in cubic phase, phase segregation is observed for x = 0.2 [20,21] as per literature data. Similarly, secondary phase formation is reported for different systems at x = 0.15 for $Ce_{1-x}Sn_xO_2$ [22], x = 0.3 for $Ce_{1-x}Lu_xO_2$ and $Ce_{1-x}Sm_xO_2$ binary oxide systems [21]. The variation in the region of solid solution formation exists significantly with the change in synthesis procedure and reaction conditions of the sample.

Apart from phase formation, other parameters that influence the catalytic activity of the selected materials, such as morphology, are also analysed and discussed in detail. The synthesised metal oxides are adopted as a catalyst for soot oxidation activity study. A single synthesis method and heat treatment condition are adopted for the better comparison of the activity of metal oxides at different compositions. To the best of our knowledge, CeO_2-HfO_2 over the whole composition was not analysed for its structural properties and specifically upon the phase changes and its influence on catalytic activity.

2. Experimental details

2.1. Materials

Nano-crystalline binary metal oxide samples of CeO_2-HfO_2 at varying composition were synthesised using the EDTA-Citrate method. Metal precursor salts of AR grade used for synthesis were Cerium nitrate hexahydrate ($Ce(NO_3)_3.6H_2O$) ≥ 99% (SRL chemicals) and Hafnium chloride ($HfCl_4$) (Aldrich), respectively. Apart from these, other chemicals used are, Ammonium hydroxide solution NH_4OH (25% ammonia) (spectrum reagents), Ethylenediamine tetra acetic acid (EDTA) ≥99% (SRL chemicals) and citric acid monohydrate ≥99% (SRL chemicals). Stoichiometric ratios of metal precursors were added in such a way that the composition of HfO_2 on CeO_2 varies from 0 to 100 mol % with 10 mol % difference between each sample. Synthesis procedure of EDTA-Citrate complexing method was followed as reported previously [16,23]. Oven drying of the obtained gel at 150 °C/24 h resulted in the formation of black precursor solid. Further, two-stage calcinations at 350 °C/12 h and 600 °C/5 h were carried out to get the corresponding metal oxide nanomaterials. The obtained metal oxides, $Ce_xHf_{1-x}O_2$ (where x = 0.0–1.0) was represented as CH_x where x varies from 0 to 100 where, CH0 and CH100 correspond to CeO_2 and HfO_2, respectively.

2.2. Characterization of catalyst

The CH_x sample diffractogram was measured using XPERT Pro diffractometer with the operating parameters of 20-80° 2θ range, 0.02 step size and 2 s step time at 40 kV and 30 mA. The radiation source used for the X-ray Diffraction (XRD) measurement was Cu Kα (0.154 nm). Debye-Scherrer equation was used to calculate the average crystallite size of the particles and the lattice constant for different phase was calculated using Bragg's law. N_2 physisorption in a SMART-SORB-92/93 instrument was done to evaluate the BET (Brunauer-Emmett-Teller) Surface area and pore volume of synthesised samples. The samples were evacuated at 150 °C/3 h before the analysis to remove residual moisture. Further, the surface area was calculated using BET method. Bruker: RFS 27 model Raman spectrometer was used to measure the Raman spectra of CH_x samples using a conventional backscattering geometry with charged-couple device (CCD) detector consisting of a triple polychromator. Diode laser source used is of a near-infrared 785 nm laser with a nominal output of 12.5 mW. Scanning Electron Microscopy/ Energy Dispersive X-ray spectroscopy (SEM/EDS) analysed in a CARL ZEISS SIGMA instrument for the microstructural and compositional analysis of the samples. High-resolution Transmission Electron Microscopy (TEM) of the samples were analysed in Joel/JEM 2100. UV–vis Diffuse Reflectance spectroscopy (UV–vis DRS) measurements were performed using a Cary 5000 UV–vis NIR spectrometer with an integration sphere diffuse reflectance attachment. Direct optical bandgap values of the samples were calculated using Tauc's plot [24]. XPS spectra was obtained using Omicron ESCA + under ultra-high vacuum with an anode of 25 W and 15KV power and Al Kα monochromator at a background pressure of 6.7×10^{-8} Pa. C 1 s peak is used to calibrate spectra obtained for all the samples. The O 1 s spectra were deconvoluted using CasaXPS software.

2.3. Soot oxidation activity measurement

All synthesised binary CH_x metal oxide samples were used as a catalyst for soot oxidation reactions and analysed in a TG/DTA 6300 TGA instrument. Printex®U (Orion Engineered Carbons) was used as the standard soot for this study. Soot and catalyst at a fixed ratio of 1:4 was premixed in a mortar for 30 min under tight contact condition. Tight contact condition was adopted in this study to analyse the intrinsic property of the catalyst. Soot oxidation reaction was analysed in the temperature range of 200–600 °C heating at 10 °C/min of heating rate in the presence of air as a purge gas at a flow rate of 100 ml/min. Samples were preheated at around 100 °C to remove moisture content bound on the sample surface [16,25]. The weight loss associated with the soot oxidation reaction was obtained from TG results and further calculated in terms of conversion. The temperature at which 50% conversion of soot occurs was used for the evaluation of the catalytic activity. The catalytic reproducibility for the soot oxidation reaction was analysed for all the samples.

The soot and catalyst mixture was analysed for Isothermal-Time-on-stream (ITOS) analysis in a TGA instrument. The sample under consideration is loaded into TGA instrument, and the sample is heated from room temperature to 420 °C under an inert condition of nitrogen flow at 100 ml/min. Once the temperature is attained, it is maintained constant, and further air is allowed at a flow rate of 100 ml/min to observe the stability of catalyst. The analysis is undergone until the reaction is fully completed. The weight loss was expressed in terms of conversion with time. The derivative (dX/dt) of conversion (X = conversion) with respect to time obtained from ITOS analysis was calculated further to find the soot oxidation reactivity in terms of $mg/g_{initial}.s$ [26].

3. Results and discussion

3.1. X-ray diffraction (XRD) analysis

Pre-calcined CH10 sample synthesised by the EDTA-Citrate method, oven dried at 150 °C/24 h is undergone TG-DTG analysis (see Supplementary file Fig. S1) to find the decomposition behaviour with the rise in temperature before the characterization of the sample. XRD analysis of the CH_x binary sample series was undergone, and Fig. 1 **(a)**

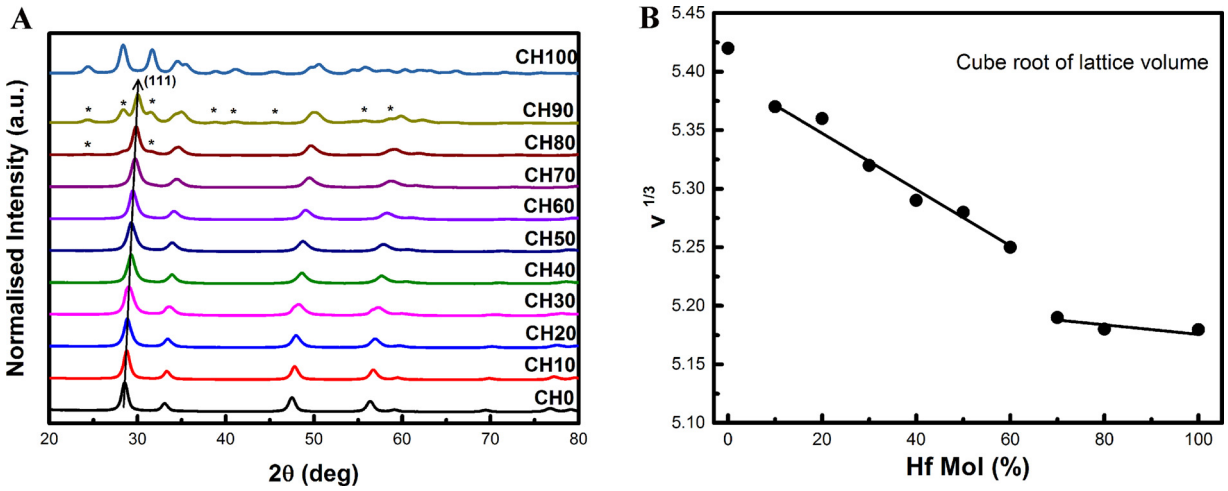

Fig. 1. (a) XRD pattern and (b) Vegard rule obtained from the lattice constant of CH_x samples calcined at 600°C/5 h.

depicts the corresponding diffraction patterns. CH0-CH90 samples demonstrate the peak corresponding to fluorite (F) phase of CeO_2 [25]. CH100 exists in monoclinic phase (M phase) of HfO_2 [27], and the monoclinic peak is evident from CH80 onwards in trace amounts. From the preliminary XRD study, multi-phase is present among the selected sample series, that is F phase (CH0 ~ CH70), hybrid phase of F and M (CH80 ~ CH90) and M phase (CH100), respectively. The lattice constants are calculated using Bragg's law for F phase (CH0-CH90) and M phase (CH100). Fig. 1 **(b)** gives the plot of cubic root of lattice volume with the dopant concentration in mole percent. The lattice constant is decreasing linearly with the increase in dopant content due to the smaller ionic radius of Hf^{4+} when compared to Ce^{4+} [28,29]. However, the slope of the line varies from CH70 onwards which indicates the solid solution is formed only up to CH70 sample as per Vegard's rule [31]. Further, with the increase in dopant content, it is no more soluble in the host lattice. Instead, it segregates as a secondary phase. This result corroborates with the peak identified from the diffraction pattern [30,32,36].

Table 1 shows crystallite size (D) and lattice strain (ε), BET surface area (S_{BET}), equivalent particle size (PS), pore volume (PV) and degree of agglomeration (ϕ) calculated for CH_x samples. D and ε value is in the range of 7.4 to 11.5 nm and 0.011-0.019, respectively. With the decrease in crystallite size, lattice strain increases and thus the oxygen diffusion may increase [8]. S_{BET} of the sample is around 18 ~ 41 m^2/g. Among the solid solution sample range obtained from XRD, CH10 showed the highest surface area compared to other samples. PS values are in the range of 19 ~ 40 nm. PV of the sample is in the range of 0.027 ~ 0.054 cm^3/g. PV decreases up to CH20 sample, further addition of dopant leads to increase in PV. Effect of PV on catalytic activity can be neglected since the pore of this range can no longer accommodate the bigger soot particles [25]. 1.6 ~ 5.0 is the degree of agglomeration (ϕ) value range of CH_x samples. Lesser agglomerated particles ensure efficient surface to volume ratio and thus enhance the catalytic activity [33]. CH10 showed lower degree of agglomeration value among the solid solution sample of CH10-CH60. A solid solution metal oxide has better thermal stability and redox properties compared to secondary phase segregated non-homogeneous mixed oxide sample [5]. Thus further analysis is required to endorse the secondary phase trend observed from XRD and correlate the activity, hence Raman spectroscopy is used.

Table 1
Crystallite size, Lattice strain, BET surface area, particle size, pore volume and degree of agglomeration of CH_x metal oxides calcined at 600°C/5 h.

Metal oxide	Crystallite size [a] (nm)	Lattice strain [b]	BET Surface area (m^2/g)	Particle size [c] (nm)	Pore volume (cm^3/g)	Degree of agglomeration [d]
CH0	10.6	0.013	41	19	0.054	1.6
CH10	9.6	0.014	29	26	0.043	2.8
CH20	8.4	0.016	19	40	0.027	4.7
CH30	7.4	0.019	24	31	0.034	4.1
CH40	8.1	0.016	18	40	0.032	4.9
CH50	7.6	0.018	21	32	0.035	4.2
CH60	8.1	0.016	20	34	0.033	4.1
CH70	7.8	0.017	25	26	0.043	3.3
CH80	8.8	0.015	20	32	0.043	3.6
CH90	11.3	0.011	25	25	0.036	2.2
CH100	9.6	0.015	21	30	0.040	3.1

[a] Crystallite size calculated using Debbye Scherrer equation.
[b] Lattice strain calculated from XRD peaks.
[c] Particle size calculated from BET Surface area.
[d] Degree of agglomeration calculated as the ratio of particle size calculated using BET surface area and crystallite size.

3.2. Raman spectroscopy analysis

From the Raman spectroscopy results obtained, the whole composition is divided into three regions based on the phase in which they exist. The Raman spectra obtained for CH_x samples are provided in Fig. S2. The dominant peak at 462.8 cm^{-1} (F_{2g}) owing to the symmetric stretching mode of F phase CeO_2 is evident in CH0 sample [33]. Thus, CH10-CH30 is considered to exist in single F phase since there is no presence of any other impurity phases. Reduction in Raman peak intensity for higher dopant content samples could be related to the difference in polarizability of Ce and Hf due to the difference in size [34]. The Raman spectrum of CH40-CH80 sample shows peak at around 260 cm^{-1} and 630 cm^{-1}, which is an indication of the presence of M phase ($P2_1$) apart from the F_{2g} peak [27]. Co-existence of peaks corresponding to both F phase CeO_2 and M phase HfO_2 confirms the formation of hybrid phase among the selected region of CH40-CH80. Raman band corresponding to vibration mode of monoclinic HfO_2 are evident for CH90 and CH100 samples [28,35]. However, only CH100 exist in pure M phase and the CH90 sample exhibits in both F and M phase in XRD results.

Chavan et al. [36] and Izu et al. [10] have synthesised Ce-Hf series at varying concentration and found that $Ce_{0.85}Hf_{0.15}O_2$ sample onwards monoclinic phase of HfO_2 starts appearing [10]. Also, weak monoclinic phase starts segregating from $Ce_{0.74}Hf_{0.26}O_2$ onwards as per study the Raitano et al. [37]. However, in the present work, the bi-phasic metal oxide in fluorite and monoclinic phase starts from CH40 based on the secondary peak from Raman result. The significant variation in phase boundaries might be due to the difference in calcination temperature,

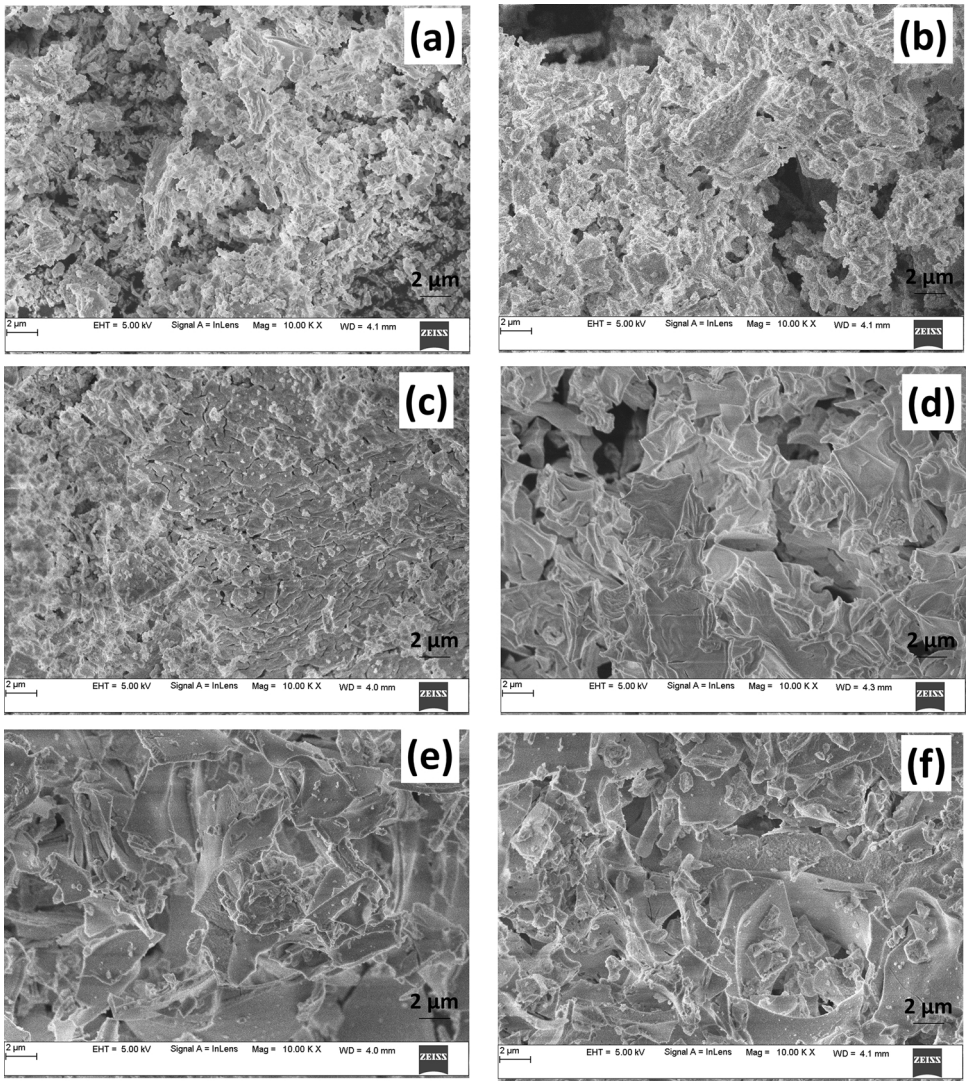

Fig. 2. SEM image of (a) CH0; (b) CH10; (c) CH20; (d) CH40; (e) CH80 and (f) CH100 samples calcined at 600°C/5 h.

crystallite size and surface area that are influenced by the adopted synthesis method. Since the secondary phase is confirmed, the effect of structural morphology upon a change in phase is analysed in further.

3.3. Scanning electron microscopy (SEM)-energy dispersive x-ray spectroscopy (EDS) analysis

Fig. 2 shows the SEM morphology of CH_x sample series. All the samples have agglomerated particles. Fig. 2**(a)** confirms the flaky agglomerated particles of CH0 sample. The flaky morphology is consistent in the case of CH10 **(**Fig. 2**(b))**, CH20 (Fig. 2**(c))** and CH30 (Fig. S3 (b)) samples that exist in single F phase. However, in case of CH40 sample in Fig. 2**(d)**, the morphology is changed considerably with the appearance of layers of flakes, which can be directly correlated to the phase variation. As the dopant content is increased further, there is not much variation in the morphology of the sample as evident for CH80 and CH100 sample in Fig. 2**(e)** and **(f)**, respectively. The SEM images of all other samples are provided in Fig. S3. Apart from the phase separation from crystallographic and vibrational results, morphological classification can also be done from the SEM image as F phase, hybrid phase and M phase in the range of CH10 ~ 30, CH40-CH90 and CH100 respectively. The EDS composition of all the samples was analysed and tabulated in Table 2 asserts that the theoretical and actual composition of the samples is almost similar.

Table 2
Band gap, composition, $(O_\beta/(O_\alpha+O_\beta+O_\gamma))$ and T_{50} temperature of CH_x metal oxides calcined at 600°C/5 h.

Metal oxide	Band Gap [a] (eV)	Composition from EDS [b] (mol %)		$O_\beta/(O_\alpha+O_\beta+O_\gamma)$ [c] (%)	T_{50} (°C)
		Ce	Hf		
CH0	3.08	100	0	41	530
CH10	2.97	92	8	44	430
CH20	2.93	82	18	34	435
CH30	2.88	76	24	36	435
CH40	2.71	65	35	58	455
CH50	2.70	52	48	36	460
CH60	2.73	47	53	32	475
CH70	2.78	35	65	43	475
CH80	2.83	26	74	36	510
CH90	2.94	11	89	45	540
CH100	5.30	0	100	54	483

[a] Calculated from UV–vis DRS using Tauc's plot.
[b] Composition calculated from EDS analysis.
[c] Area ratio obtained from O 1 s peak of XPS analysis using CasaXPS software.

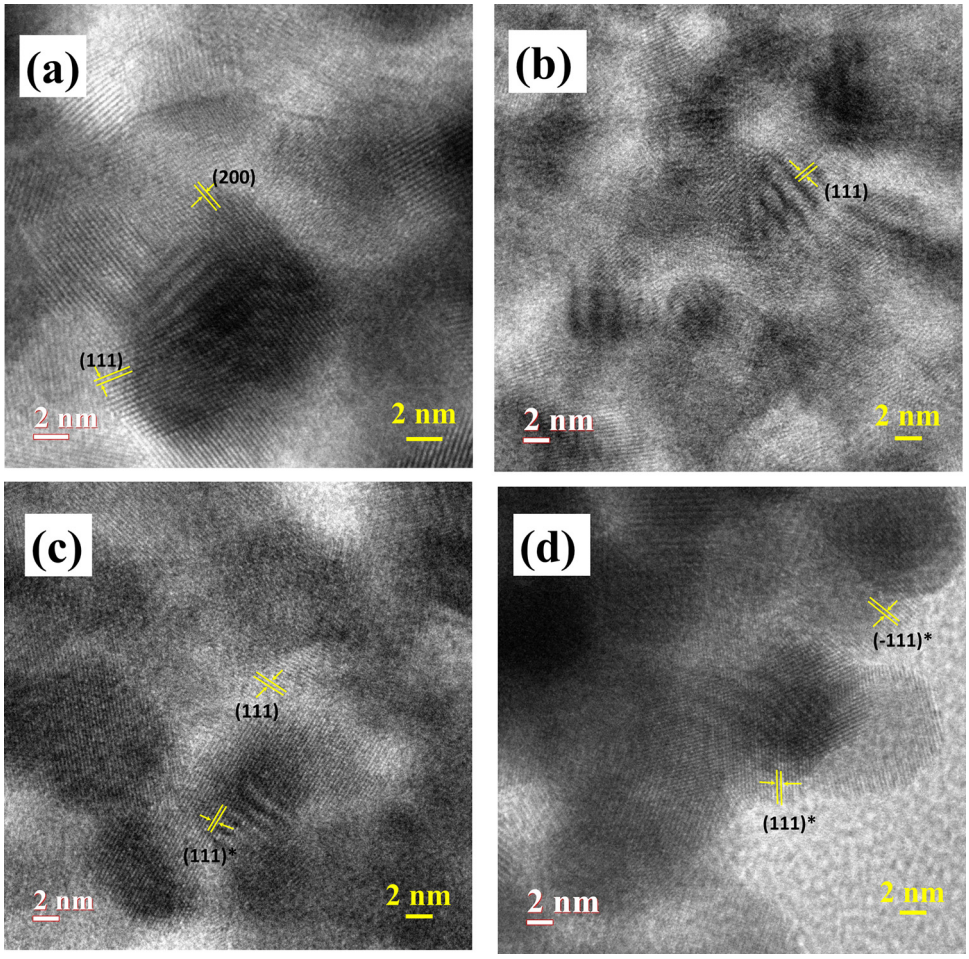

Fig. 3. HR-TEM of (a) CH10; (b) CH40; (c) CH80 and (d) CH100 samples calcined at 600°C/5 h. *Represent the planes in monoclinic phase.

3.4. Transmission Electron microscopy (TEM) and selected area Electron diffraction (SAED) analysis

HR-TEM images in Fig. 3 shows the lattice fringes corresponding to each plane. CH10 and CH40 sample fringes corresponds to the d spacing of (111) plane in F phase as indicated in the Fig. 3**(a)** and **(b)**, respectively. CH10 has an additional presence of more reactive facet plane of (200). These planes may be formed by defect creation while doping that may aid in the active site availability [14]. CH80 in Fig. 3**(c)** shows the lattice fringes corresponding to the d spacing of intense peaks in both F and M phase, which strongly confirms the existence of hybrid phase in this sample. However, CH100 indicates only the planes in M phase as shown in Fig. 3**(d)**.

SAED pattern of all the samples confirms polycrystalline nature of the sample (see Fig. S4). CH10 sample with clear concentric smooth rings confirms fluorite phase of CeO_2 as calculated from XRD result with each circle corresponding to each plane [38]. For CH40 sample, few spots start appearing in the ring pattern corresponding to the monoclinic phase of HfO_2 [39]. However, the rings are not precise; instead, crystals are seen as spots of almost similar size to that of CH10. Apart from larger spots, some smaller spots are also evident which may correspond to that of dopant. On observing the SAED pattern of CH80 sample the spot size reduction occurs which are similar to smaller spots in CH40 sample. The crystals are not well arranged in ring form. CH100 sample shows spots similar to that of CH80, but of lesser in number, the ring structure is not well maintained in this case. Thus, it is clear from the electron diffraction images that CeO_2 exist in ring pattern with larger spots and HfO_2 maintains the spot pattern with smaller spots [40,41]. In case of CH40 sample, ring pattern is almost maintained with both larger and smaller spots corresponding to host and dopant, respectively, confirms the hybrid phase. The hybrid phase formation affects surface morphology as evident in SEM result is consistent with the results obtained from SAED images.

3.5. UV-vis diffuse reflectance spectroscopy (UV–vis DRS) analysis

To study the optical bandgap and electronic structure of metal ions, UV–vis DRS analysis is undergone. Based on the UV–vis DRS results obtained (see Supplementary information Fig. S5), all sample (except CH100) shows two peaks around 270 and 345 nm in CH0 spectra corresponds to charge transfer transition and interband transition as per the literature [40,41]. Absorption peak in UV region at around 245 nm is only seen in CH100 sample that essentially corresponds to HfO_2 [42]. Substitution of Hf^{4+} into the CeO_2 lattice consequently results in strain development at the Ce sites due to lowering of symmetry [43]. optical bandgap has a direct correlation with the oxygen vacancy, lattice distortion and surface defects [27]. Using Tauc's plot [24], the optical bandgap value for all CH_x samples are calculated as shown in Fig. 4 and tabulated in Table 2. With respect to the variation in phase formation, the effect of optical bandgap may also change. The detailed analysis of optical bandgap will be discussed in further.

3.6. X-ray photoemission spectroscopy (XPS) analysis

The O 1 s spectra of CH_x samples in single phase and hybrid phase obtained from XPS data is shown in Fig. 5**(a)** and **(b)**, respectively. The peaks obtained in O 1 s matches well with the literature [46]. Peaks obtained in O 1 s can be assigned to lattice oxygen (O_α), surface oxygen

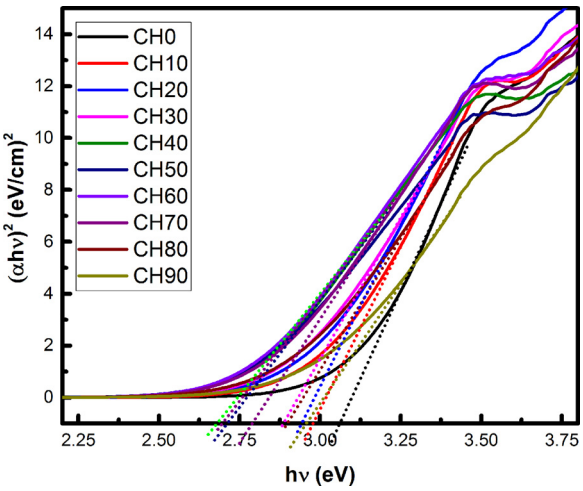

Fig. 4. (a) UV–vis DRS of CH_x samples calcined at 600°C/5 h.

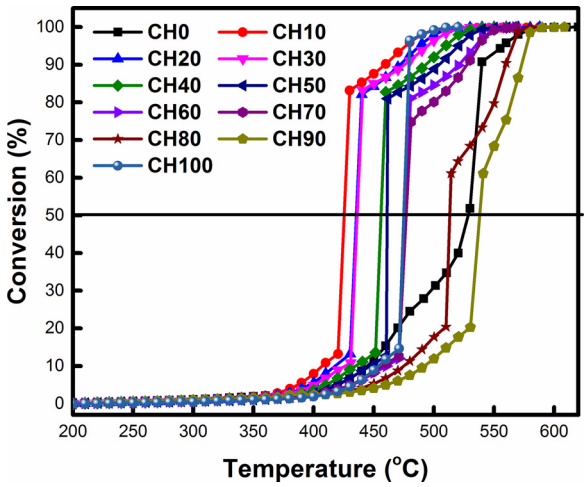

Fig. 6. Soot conversion profile of CH_x samples calcined at 600°C/5 h.

(O_β) and oxygen due to hydroxyls (O_γ) [47]. Using CasaXPS software, the peaks were deconvoluted and the ratio of surface oxygen concentration to the total oxygen concentration, i.e., $(O_\beta/(O_\alpha + O_\beta + O_\gamma))$ is obtained and tabulated in Table 2. For the F phase samples (CH10 ~ CH30) and for hybrid (F + M) phase (CH40 ~ CH90), the $(O_\beta/(O_\alpha + O_\beta + O_\gamma))$ is obtained in the range of (34–44%) and (32–58%), respectively. Among the F phase samples, CH10 sample and among hybrid phase, CH40 sample showed better $(O_\beta/(O_\alpha + O_\beta + O_\gamma))$ values and it may also influence the soot oxidation activity [4] apart from phase, surface morphology and optical bandgap.

3.7. Soot oxidation activity

Fig. 6 depicts the soot conversion profile of all the samples with rise in temperature and Table 2 provides the T_{50} temperature data corresponding to each sample. From the conversion plot, it is evident that the activity is relatively higher for F phase (CH10-CH30) samples rather than the hybrid (F + M) and M phase samples. Among F phase samples, CH10 (430 °C) displayed the lowest T_{50} temperature followed by CH20 and CH30 respectively. Also the order of catalytic activity in hybrid phase samples are CH40 > CH50 > CH60 ~ CH70 > CH80 > CH90 respectively. A preliminary characterisation study, such as XRD and Raman spectroscopy and also the surface morphology study using SEM and SAED analysis has shown the evidence of hybrid phase from CH40

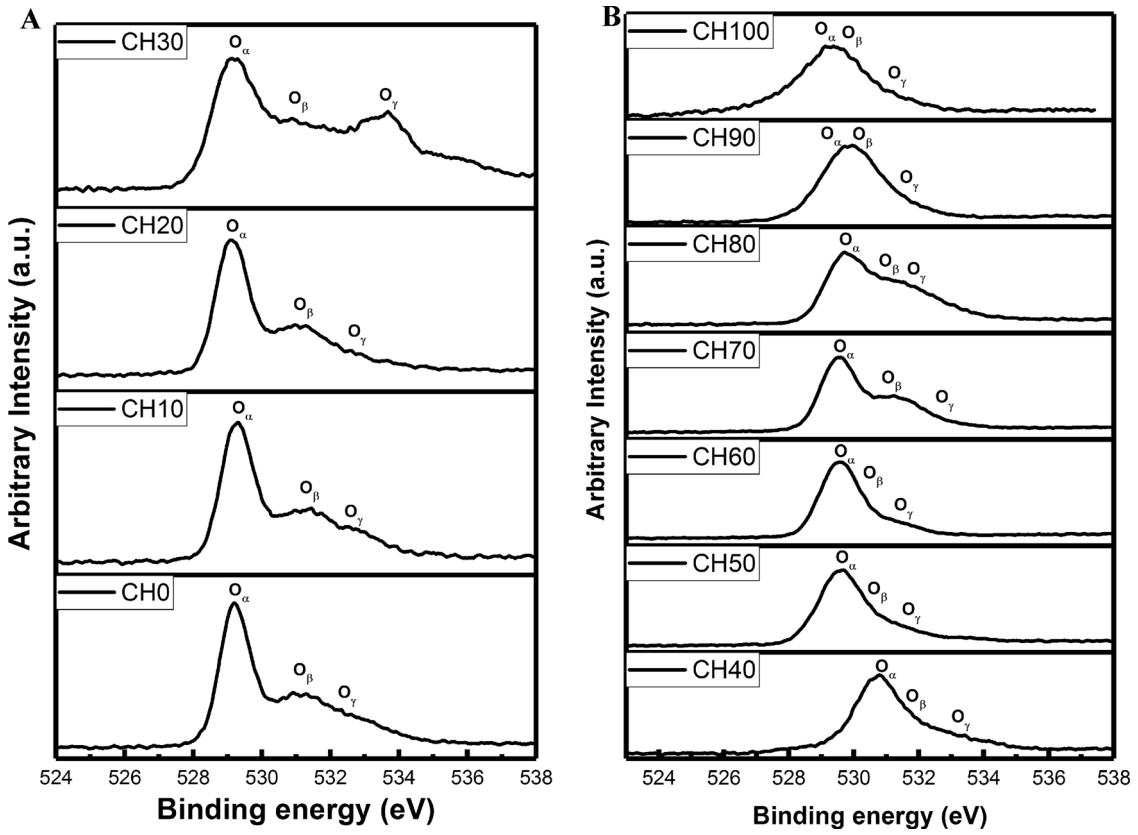

Fig. 5. O 1s XPS of (a) CH0 ~ 30 and (b) CH40-CH100.

Table 3
Summary of lattice strain, BET surface area, degree of agglomeration, band gap and T_{50} temperature of CH_x series in different phases.

Metal Oxide	Phase	Lattice strain	BET Surface area (m^2/g)	Degree of agglomeration	Band Gap (eV)	T_{50} (°C)
CH0	Pure Fluorite	0.013	41	1.6	3.08	530
CH10-CH30	Fluorite	0.014-0.019	19-29	2.8-4.7	2.88-2.97	430-435
CH40-CH90	Fluorite + Monoclinic	0.011-0.018	18-25	2.2-4.9	2.70-2.94	460-540
CH100	Pure Monoclinic	0.015	21	3.1	5.30	483

sample onwards. From this study, a preliminary conclusion can be made that, catalytic activity depends highly upon the composition and structural morphology of the material. As the morphology of the catalyst varies, the active contact site for soot oxidation is reduced and thus it affects the activity of the sample. Apart from that, phase formation also affects the active contact points for the soot oxidation reaction. Summary of different parameters obtained for all the samples based on the phase of existence is given in Table 3. Fig. S6 (a) shows the effect of contact mode (tight and loose) on soot oxidation activity of CH0 sample and tight contact mode resulted in better catalytic activity than the loose contact mode. In tight contact mode, the intrinsic property of the catalyst sample controls the soot oxidation reaction and results in better catalytic activity than compared to loose contact mode [25,48]. Fig. S6(b) shows the effect of soot to catalyst ratio (1:4 and 1:10) on the soot oxidation activity of CH10 sample in tight contact mode. As the soot to catalyst ratio is increased from 1:4 to 1:10 there is an increase of catalytic activity and this can be due to increase in the contact points of the soot and catalyst sample [49]. As the soot to catalyst ratio is changed from 1:4 to 1:10, the catalytic activity is increased by only 9 °C. Based on the literature [16,25] and the results obtained from the present study the repeated tests were carried out for the CH_x samples in tight contact mode at soot to catalyst ratio of 1:4 (See Fig. S7 in Supplementary information) and results showed that the change in the catalytic activity trend is same.

Reddy et al. [12] synthesised CeO_2-HfO_2 of 80:20 mol ratio using coprecipitation method under a calcination temperature of 500 °C/5 h obtained a soot activity at 409 °C as T_{50} temperature which is quite lower when compared to same composition (435 °C) prepared in this study. This might be due to difference in synthesis method, calcination temperature which resulted in lower crystallite size (5 nm) and higher surface area (78 m^2/g) of those samples compared with sample prepared in the present study.

Fig. 7**(a)–(c)** shows the variation in T_{50} temperature with the deviation in crystallite size, optical bandgap and lattice strain, respectively. From the trend, it is clear that the activity is nearly similar to the variation in these parameters in hybrid (F + M) phase region. The lowering of catalytic activity points out the substantial influence of structural properties instead of intrinsic properties apart from the hybrid phase existence. Morphology of the sample significantly varies along with the secondary phase formation. Thus, the active sites on the catalyst surface are depleted for soot oxidation due to the hindering of redox (Ce) ions by the non-redox (Hf) ions. Lattice strain developed in the crystal decreases since the defect creation in host lattice is reduced due to a decrease in dopant available within the crystal structure. As the lattice strain decreases, the oxygen mobility within the catalyst is reduced that results in a decrease in catalytic activity [7,8]. With the reduction in crystallite size lower reducibility energy is achieved [44,33]. Conversely, in case of solid solution samples, CH10 with the minimum dopant content exhibited the highest activity. CH10 showed the highest surface area, smaller particle size, lower degree of agglomeration and higher (O_β/ ($O_\alpha + O_\beta + O_\gamma$)) value within F phase samples (CH10-CH30) that aids in improving surface properties of the samples which in turn enhances the catalytic activity [50,51].

3.8. Isothermal-time-on-stream (ITOS) analysis

The Isothermal-Time-on-stream (ITOS) analysis of CH0, CH10, CH40, CH80 and CH100 was undergone at the specific reaction condition and shown in Fig. 8**(a)**. Under nitrogen condition, there is no significant weight loss in the samples, except for CH0 samples. The weight loss for CH0 is due to the high redox potential (Ce^{3+}/Ce^{4+}) of CeO_2. During isothermal reaction, weight loss due to soot oxidation is considerably low and reaction rate is preliminary dependent upon catalytic activity [45]. The conversion with respect to time under the air flow provides an idea about the time required for each catalyst to undergo complete oxidation. Similar to the T_{50} trend observed previously in non-isothermal condition, the catalytic activity of CH10 sample is highest and CH80 showed the lowest activity. In case of CH100, the activity is considerably better than CH80 sample. CH40 and CH10 showed almost same activity but the non-isothermal result was the other way. This can be related to the weight loss occurring even under N_2 flow which is inert in case of other samples. Observed isothermal variation can be attributed to the catalytic activity of the samples. CH10 is highly stable with higher catalytic activity out of all CH_x samples studied which has the potential to exploit further. The reaction rate of the samples are calculated from the conversion plot and given in Fig. 8**(b)** [26]. Rate of reaction is in the order of 0.05–1.0 $mg/g_{initial}.s$. Similar to the previous observation, reaction rate is higher for CH10 (1.0 $mg/g_{initial}.s$) sample followed by CH40 (0.4 $mg/g_{initial}.s$) and CH100 (0.25 $mg/g_{initial}.s$) sample. CH80 (0.08 $mg/g_{initial}.s$) has the lowest activity among all the samples. Reactivity rate follows the same trend as that of T_{50} obtained for soot activity of the samples.

4. Conclusions

Binary metal oxide of CH_x over whole composition range was synthesised using the EDTA-Citrate method and calcined at 600 °C/5 h. The metal oxides characterised by XRD analysis confirms the existence of different phases based on peaks and Vegard's rule (lattice constant (5.15–5.41 Å)) as fluorite (F), hybrid (F + M) and monoclinic (M) phases. Raman spectroscopy asserts the phase boundary of hybrid phase from CH40. With the change in phase from single to hybrid, the morphology of the sample also varies substantially as per SEM morphological analysis. It is further supported by the variation in SAED pattern of the samples. Soot oxidation study under tight contact condition confirms that the catalytic activity is higher for solid solution samples in F phase CH10-CH30 (430–435 °C) rather than the hybrid phase CH40-CH100 samples (450–560 °C). The textural and structural properties supports the catalytic activity of F phase samples. The T_{50} temperature, as low as 430 °C is obtained for CH10 is due to enhanced structural properties such as high surface area, low particle size, degree of agglomeration and higher surface oxygen concentration that improves the contact points, apart from stable morphology and phase. As far as soot oxidation is concerned, the descriptors that controls the catalytic activity for CH_x samples can be generalised as stable solid solution formation with stable host structure, optimum dopant concentration and stable structural properties. Soot oxidation being significantly controlled by structural properties, improvement in structural features is critical in enhancing the activity.

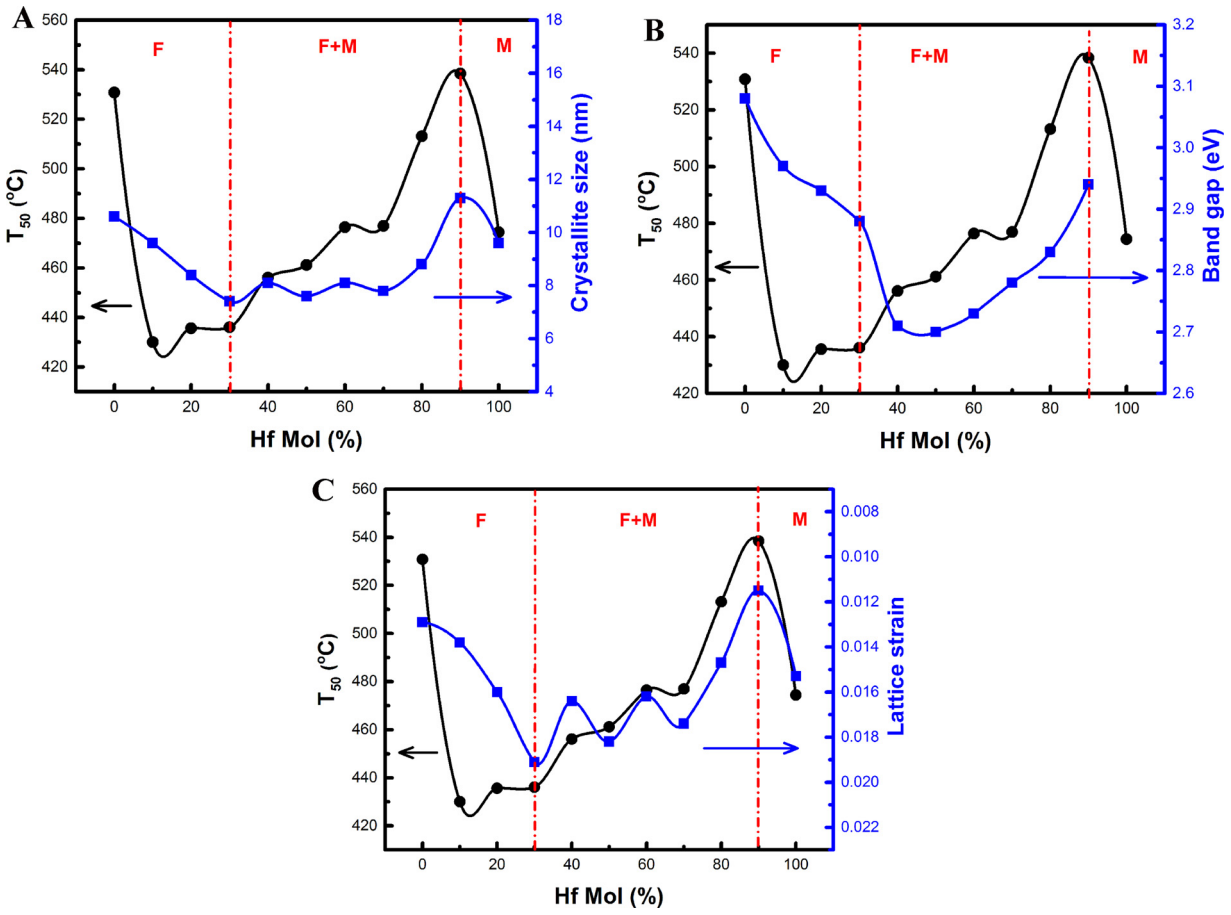

Fig. 7. Comparison of T_{50} with (a) Crystallite size; (b) Band gap and (c) Lattice strain of CH_x samples calcined at 600°C/5 h.

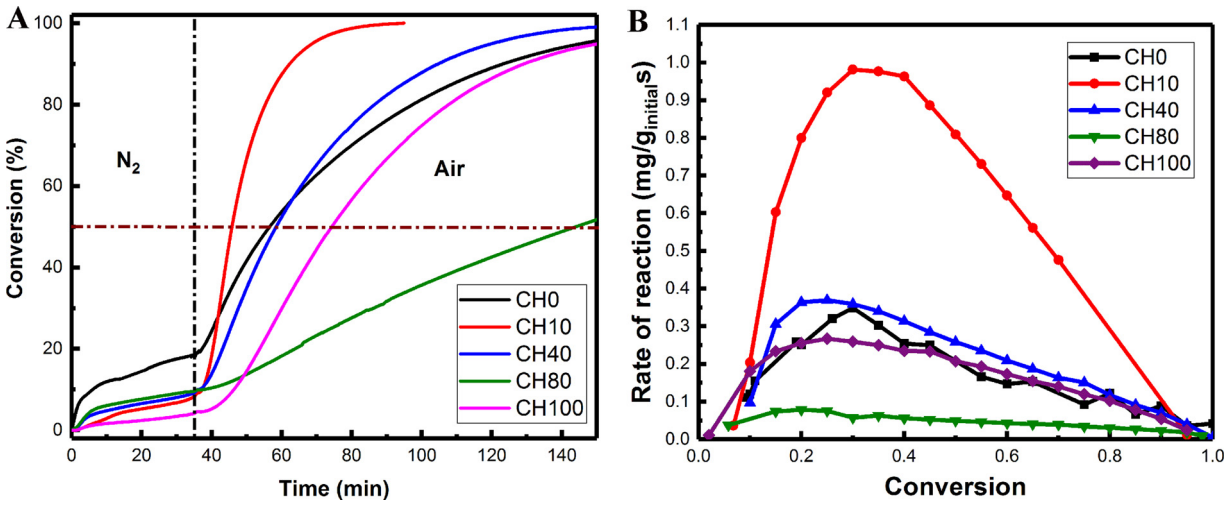

Fig. 8. (a) Isothermal time study of CH0, CH10, CH40, CH80 and CH100 sample for soot oxidation reaction (b) corresponding reaction rate of samples vs. conversion.

Authors contribution

All the experimental data are obtained and analysed by APA, HPD perceived the whole study. XRD data was provided by UBB and BET surface area, pore volume was provided by HD. All the authors contributed to writing and editing the document.

Acknowledgements

The project has been funded by DST INSPIRE Project (IFA-13 ENG-48). We thank MRC, MNIT Jaipur for facilitating XPS and Raman Spectroscopy data. We acknowledge SAIF STIC, Cochin for UV-vis DRS and TEM data and also Mangalore University for SEM-EDS data.

Appendix A. Supplementary data

Supplementary material related to this article can be found, in the online version, at doi:https://doi.org/10.1016/j.apcata.2018.08.019.

References

[1] A. Trovarelli, Comments Inorg. Chem. 20 (1999) 263–284.
[2] T. Vinodkumar, B.G. Rao, B.M. Reddy, Catal. Today 253 (2015) 57–64.
[3] M. Capdevila-Cortada, G. Vile, D. Teschner, J. Perez-Ramirez, N. Lopez, Appl. Catal. B Environ. 197 (2016) 299–312.
[4] A. Bueno-López, K. Krishna, M. Makkee, J.A. Moulijn, Catal. Letters 99 (2005) 203–205.
[5] C. de Leitenburg, A. Trovarelli, F. Zamar, S. Maschio, G. Dolcetti, J. Llorca, J. Chem. Soc. Commun. 2 (1995) 2181–2182.
[6] R. Di Monte, J. Kašpar, Catal. Today 100 (2005) 27–35.
[7] D. Ma, Z. Lu, Y. Tang, T. Li, Z. Tang, Z. Yang, Phys. Lett. A 378 (2014) 2570–2575.
[8] M.J.D. Rushton, A. Chroneos, S.J. Skinner, J.A. Kilner, R.W. Grimes, Solid State Ion. 230 (2013) 37–42.
[9] B.M. Reddy, P. Bharali, P. Saikia, A. Khan, S. Loridant, M. Muhler, W. Grünert, J. Phys. Chem. C 111 (2007) 1878–1881.
[10] N. Izu, T. Itoh, W. Shin, I. Matsubara, N. Murayama, Sensors Actuators B Chem. 123 (2007) 407–412.
[11] K. Karakaya, A. Zinine, J.G.M. van Berkum, M.A. Verheijen, Z.M. Rittersma, G. Rijnders, D.H.A. Blank, J. Electrochem. Soc. 153 (2006) F233.
[12] B.M. Reddy, P. Bharali, T. Gode, P. Saikia, K. Lakshmi, S.-E. Park, Catal. Letters 123 (2008) 327–333.
[13] T. Vinodkumar, D. Durgasr Naga, B.M. Reddy, Int. J. Adv. Eng. Sci. 5 (2013) 224–231.
[14] P. Bharali, G. Thrimurthulu, L. Katta, B.M. Reddy, J. Ind. Eng. Chem. 18 (2012) 1128–1135.
[15] A.S. Foster, F. Lopez Gejo, A.L. Shluger, R.M. Nieminen, Phys. Rev. B - Condens. Matter Mater. Phys. 65 (2002) 1741171–17411713.
[16] A.P. Anantharaman, H.P. Dasari, J.-H. Lee, H. Dasari, G.U.B. Babu, Catal. Letters 147 (2017) 3004–3016.
[17] N. Guillén-Hurtado, A. Bueno-López, A. García-García, J. Mater. Sci. 47 (2012) 3204–3213.
[18] R. Si, Y.W. Zhang, S.J. Li, B.X. Lin, C.H. Yan, J. Phys. Chem. B 108 (2004) 12481–12488.
[19] K.A. Pokrovski, A.T. Bell, J. Catal. 241 (2006) 276–286.
[20] V. Grover, A.K. Tyagi, Mater. Res. Bull. 39 (2004) 859–866.
[21] C. Artini, M. Pani, M.M. Carnasciali, M.T. Buscaglia, J.R. Plaisier, G.A. Costa, Inorg. Chem. 54 (2015) 4126–4137.
[22] J.L. Ayastuy, A. Iglesias-González, M.A. Gutiérrez-Ortiz, Chem. Eng. J. 244 (2014) 372–381.
[23] D.H. Prasad, S.Y. Park, E.O. Oh, H. Ji, H.R. Kim, K.J. Yoon, J.W. Son, J.H. Lee, Appl. Catal. A Gen. 447-448 (2012) 100–106.
[24] J. Tauc, R. Grigorovici, A. Vancu, Phys. Status Solidi 15 (1966) 627–637.
[25] K. Krishna, A. Bueno-López, M. Makkee, J.A. Moulijn, Appl. Catal. B Environ. 75 (2007) 189–200.
[26] C. Su, P.J. McGinn, Appl. Catal. B Environ 138-139 (2013) 70–78.
[27] M. Piumetti, S. Bensaid, N. Russo, D. Fino, Appl. Catal. B, Environ. 165 (2015) 742–751.
[28] E. Mendoza-Mendoza, J.S. Quintero-García, B.A. Puente-Urbina, O.S. Rodríguez-Fernández, L.A. García-Cerda, J. Alloys Compd. 692 (2017) 448–453.
[29] H. Padma Kumar, S. Vidya, S. Saravana Kumar, C. Vijayakumar, S. Solomon, J.K. Thomas, J. Asian Ceram. Soc. 3 (2015) 64–69.
[30] D. Devaiah, T. Tsuzuki, T. Boningari, P.G. Smirniotis, B.M. Reddy, RSC Adv. 5 (2015) 30275–30285.
[31] L. Vegard, Zeitschrift Für Phys. 5 (1921) 17–26.
[32] Z. Abbas, M. Surendran, P.A. Anjana, P.K. Jidev, H. Dasari, N. Sudhakar Naidu, S. Anandhan, K.U. Bhat, G.U. Bhaskar Babu, H. Prasad Dasari, Mater. Today Proc. 4 (2017) 9360–9364.
[33] X.L. Sun, A.I.Y. Tok, R. Huebner, F.Y.C. Boey, J. Eur. Ceram. Soc. 27 (2007) 125–130.
[34] K. Ahn, D.S. Yoo, D.H. Prasad, H. Lee, Y. Chung, J. Lee, Chem. Mater. 24 (2012) 4261–4267.
[35] C. Artini, M. Pani, M.M. Carnasciali, J.R. Plaisier, G.A. Costa, Inorg. Chem. 55 (2016) 10567–10579.
[36] S.V. Chavan, A.K. Tyagi, Mater. Sci. Eng. A 433 (2006) 203–207.
[37] J.M. Raitano, S. Khalid, N. Marinkovic, S.W. Chan, J. Alloys Compd. 644 (2015) 996–1002.
[38] X. Yao, C. Tang, Z. Ji, Y. Dai, Y. Cao, F. Gao, L. Dong, Y. Chen, Catal. Sci. Technol. 3 (2013) 688–698.
[39] B. Puente-urbina, Mater. Lett. 159 (2015) 520–524.
[40] A. Shantilal Gangrade, A. Aditya Varma, N. Kishor Gor, S. Shriniwasan, S.S.V. Tatiparti, Phys. Chem. Chem. Phys. 19 (2017) 6677–6687.
[41] Y. Mikhlin, M. Likhatski, A. Karacharov, V. Zaikovski, A. Krylov, Phys. Chem. Chem. Phys. 11 (2009) 5445–5454.
[42] D.H. Prasad, S.Y. Park, H.I. Ji, H.R. Kim, J.W. Son, B.K. Kim, H.W. Lee, J.H. Lee, J. Phys. Chem. C 116 (2012) 3467–3476.
[43] K.K. Babitha, A. Sreedevi, K.P. Priyanka, B. Sabu, T. Varghese, Indian J. Pure Appl. Phys. 53 (2015) 596–603.
[44] V. Jayaraman, S. Sagadevan, R. Sudhakar, J. Electron. Mater. (2017) 1–6.
[45] B.M. Reddy, A. Khan, Catal. Surv. Asia 9 (2005) 155–171.
[46] J. Dupin, D. Gonbeau, P. Vinatier, A. Levasseur, Phys. Chem. Chem. Phys. 2 (2000) 1319–1324.
[47] W. Zhang, X. Niu, L. Chen, F. Yuan, Y. Zhu, Sci. Rep. 6 (2016) 1–10.
[48] C. Su, P.J. McGinn, Catal. Commun. 43 (2014) 1–5.
[49] K. Leistner, A. Nicolle, P. Da Costa, (2012).
[50] H. Cordatos, D. Ford, R.J. Gorte, J. Phys. Chem. 100 (1996) 18128–18132.
[51] H. Wang, S. Liu, Z. Zhao, X. Zou, M. Liu, W. Liu, X. Wu, D. Weng, Catal. Sci. Technol. 7 (2017) 2129–2139.